Numerical Simulation of the Generation and Breaking of Internal Gravity Waves

Isidoro Orlanski and Bruce B. Ross

Geophysical Fluid Dynamics Laboratory, NOAA, Princeton University
Princeton, New Jersey 08540

A numerical model is presented that permits the simulation of stratified fluid phenomena in which gravitationally unstable regions are present. The influence of subgrid scale turbulence generation due to convective instability is parameterized by relating eddy viscosity coefficients to the local Rayleigh number in unstable regions. The model is used to study three different laboratory scale flow problems involving gravity wave generation, wave breaking, and penetrative convection. The numerical solutions show good agreement with available experimental and analytic results as well as with a numerical solution obtained by other investigators.

The importance of internal gravity waves in the fluid dynamics of intermediate and meso-scale geophysical phenomena has been recognized for some time. The significance of such waves is due in large part to their ability to transfer momentum and heat to regions far removed from their generation source. In the case of orographically induced waves, *Lilly* [1972] points out that wave drag can affect the mean flow of the atmosphere at an altitude that is far greater than the height of the mountains producing the wave system. Likewise, there is evidence that strong penetrative convection can generate internal waves of sufficient strength to alter markedly the stably stratified mean environment above the convective region. Remote sensing observations by *Gossard et al.* [1970] and *Hooke et al.* [1972] suggest that gravity waves play a major role in the dynamics of the atmospheric boundary layer during stable nocturnal conditions. *Orlanski* [1973] has recently pointed out that the diurnal oscillation of atmospheric heating will generate gravity waves of all scales up to wavelengths of the order of 400 km.

In the present paper we will present a method for numerically simulating internal gravity wave phenomena. Crucial to such a simulation is the method by which subgrid scale processes resulting from gravitational instability are modeled, since wave-breaking events are

both probable and important in most finite amplitude internal wave problems that are suited to numerical simulation. Therefore in the section on parameterization of subgrid scale gravitational instability we will present a scheme for paremeterizing the small-scale mixing, which is generated owing to local gravitational instability. Typically, such instability may occur either dynamically, when an internal wave exceeds a critical amplitude [*Orlanski and Bryan*, 1969], or thermodynamically, because of heating processes that act to reduce the density of a parcel of fluid to a value below that of the fluid parcel immediately above it. In the parameterization that follows the instabilities, which result from both dynamic and thermodynamic processes, will be treated in the same manner.

In the section on model description we will describe the basic characteristics of the numerical model, which has been used to produce the computed solutions. Then, in the three sections following this one, numerical solutions for different stratified fluid phenomena will be presented and compared with relevant numerical and experimental results. Specifically, we will treat three flow problems that are amenable to laboratory experimentation: (1) the growth of standing internal gravity waves in a rectangular container because of the resonant forcing of a paddle at the top of the container, (2) the collapse of a region of uniform density embedded in a stably stratified fluid, and (3) the pene-

tration of an isolated buoyant element into a stably stratified region and the generation of internal waves due to its motion. Of these three cases, only the last process is directly applicable to phenomena encountered in the atmosphere and ocean; however, all three are relevant to geophysical fluid dynamics. Their simulations are presented here to suggest what can be done with the present model as adapted to meet the needs of more specific geophysical processes involving gravity waves and convective instability.

Throughout this paper the variability of either salinity or temperature will be envisaged as the means by which density variations of the water medium are produced. We will find it convenient for the sake of exposition to use density and temperature interchangeably according to the extent to which each is relevant to the particular physical experiment being discussed. Thus, for example, we will refer to temperature variations in the rising bubble experiment of the section on penetration of an isolated thermal into a stably stratified fluid, and we will consider variations of density or salinity in discussing the collapse of a mixed region in the section that precedes it.

PARAMETERIZATION OF SUBGRID SCALE GRAVITATIONAL INSTABILITY

In order to simulate geophysical fluid dynamics problems through numerical integration of the relevant flow equations the scientist is often faced with the question of how to represent energy sources and sinks due to processes having scales too small to be resolved by the model. The most common method for treating these processes is to relate the subgrid eddy fluxes to the local resolved flow properties in accordance with the behavior of simple turbulent flows. (The calculation of these eddy fluxes using turbulence transport equations, such as has been done by *Daly and Harlow* [1970], *Deardorff* [1973], and others, seems to be appropriate only for treating flows in which horizontal and vertical scales are similar. The application of such methods to most mesoscale phenomena thus appears to be impractical.) It was along these lines that *Smagorinsky* [1963] obtained an expression for his general circulation model in which the horizontal eddy viscosity coefficient was taken to be propor-

tional to the local deformation of the horizontal velocity field. Formulations such as this that relate the eddy coefficient magnitude to velocity deformation alone reflect the behavior of turbulence without density stratification and as such are suitable only for neutrally stratified flows or for flows such as those treated by Smagorinsky in which buoyancy effects do not affect the turbulent transfer being modeled. However, it is important to distinguish between turbulence in a flow with completely neutral stratification (i.e., a flow in which density is the same at each point for all time) and turbulence in a flow in which stratification is neutral in the mean (i.e., density is constant over the region when it is averaged over an interval of space and time but may involve large local fluctuations). Indeed, neutral conditions in the atmosphere (as, for example, might occur near the ground at certain times of the day) must be classified in the category where stratification is neutral in the mean and as such will still involve local density fluctuations that require the inclusion of buoyancy effects in their representation.

Very important differences exist in the nature of turbulence generation between flows with completely neutral stratification and flows involving buoyancy effects. In completely neutral flows the production of turbulence will be limited to local generation by shear instability (Rayleigh instability) within the interior of the fluid, by boundary effects such as surface roughness along fluid boundaries, etc. In each case, turbulence in fluid without buoyancy will be largely confined to the vicinity of the point of generation, advection providing the only means by which the turbulence can be transported to other parts of the fluid.

In stratified fluids (including fluids that are neutrally stratified in the mean), turbulence generation can be attributed to a number of different mechanisms, as, for example, shear instability (modified by density stratification), forced and free convection, critical layer absorption, and gravity wave interaction. The number and diversity of such mechanisms for local turbulence generation must certainly strain the ability of the meteorologist to provide a single parameterization capable of representing each mechanism for generating tubulence locally.

However, stably stratified fluids allow for

an additional mechanism, namely, internal gravity wave propagation, which permits turbulence to be generated at locations that are far removed from the place where the waves were first generated. Gravity waves are initially produced by mechanisms such as penetrative convection, shear instability breakdown, orographic effects, or any other energy input at the fluid boundary. The waves so produced will then propagate through regions of stable stratification in the fluid until an abrupt change in the wave energy occurs and turbulence is generated owing to wave breaking, interaction between gravity waves, or critical layer absorption.

The question concerning us in the present section is how to model the subgrid eddy fluxes that would occur in a stratified flow due to turbulence generated by the many different mechanisms discussed in previous paragraphs. In this regard it is helpful to review several important eddy diffusivity formulations that have been devised in order to model turbulent fluxes in stratified fluids.

In studying free convection in the lower atmosphere, *Priestley* [1954] used dimensional arguments to obtain an expression for eddy diffusivity for free convection of the form

$$\kappa_e = (k\Delta z)^2(-g/\theta \, \partial\theta/\partial z)^{1/2} \qquad (1)$$

where k is an empirical constant and the relevant length scale for subgrid turbulence has been assumed here to be the vertical grid size Δz. Note that eddy viscosity has been assumed here to be independent of molecular viscosity in this turbulent atmospheric situation. More recently, *Lilly* [1962] has extended Smagorinsky's eddy viscosity formulation for a neutral atmosphere to include density stratification. The resulting expression for eddy viscosity v_e and eddy diffusivity κ_e thus includes a buoyancy term, which is similar to that proposed by Priestley and reduces to Smagorinsky's form when stratification is neutral:

$$\kappa_e = (k\Delta z)^2\left(|D_v|^2 - \gamma\frac{g}{\theta}\frac{\partial\theta}{\partial z}^{1/2}\right) \qquad (2)$$

where $|D_v|$ is the velocity deformation, the quantities k and γ are empirical constants of order unity, and κ_e and v_e have been assumed here to be equal (note that κ_e is set equal to zero for $\gamma(g/\theta)(\partial\theta/\partial z) > |D_v|^2$).

Lilly's formulation seems to be reasonable in the context of flows with weak stratification. However, there does not seem to be conclusive evidence at the present time to permit a general parameterization of the role of deformation field in convective instability processes. Indeed, some numerical experiments performed by *Lipps* [1971] for convection with vertical shear suggest that wind shear may reduce vertical transport rather than increase it as is implied by Lilly's eddy viscosity model. In fact, the great diversity of mechanisms that exist for generating turbulence in stably and unstably stratified flows (as were described earlier in this section) suggests that no simple correlation exists between turbulence generation and velocity deformation in flows involving significant buoyancy effects. Because of the uncertainties that still exist in our understanding of the role of velocity shear in affecting the general turbulence generation event in a stratified fluid it would seem to be reasonable at the moment to exclude velocity deformation dependence from our parameterization of turbulent fluxes. Thus, since all the fluids with which we will be dealing here involve significant buoyancy effects (including stratification that is neutral in the mean), we have chosen only to increase eddy viscosity above molecular values in the present laboratory studies (or above background values in atmospheric models) for local regions where density gradients become gravitationally unstable. Such a choice of eddy viscosity formulation is in keeping with our interest in the growth, interaction, and breaking of internal gravity waves; in addition, it is supported by the suggestion of *Orlanski and Bryan* [1969] and *Orlanski* [1971] that the breaking of internal gravity waves by gravitational instability may be a major mechanism for turbulence generation in the deep ocean.

In fact, although only gravity wave overturning and convection processes are directly parameterized by this gravitational instability formulation, the assumed eddy viscosity will still model turbulence generation due to shear instability to the extent that such instability is resolved by the numerical model. In unstable conditions, convection processes will produce turbulent eddy fluxes directly through the formulation, whereas shear effects will alter this condition to the extent that they alter the im-

posed density gradient in the convection region. On the other hand, when the stratification is stable or neutral in the mean, strong shear in regions of low positive Richardson number will produce local instability when conditions are favorable. This instability will then grow until local overturning occurs and thereby activates the eddy viscosity in that region and damps out further growth. The gravitational instability condition thus serves to quench resolved shear instability in stratified flows as well as to model subgrid eddy fluxes produced by this shear instability. Before describing the specific eddy viscosity formulation to be used we will briefly discuss the generation of turbulence due to the wave-breaking process.

Previous studies [*Orlanski and Bryan*, 1969; *Orlanski*, 1971, 1972] have been carried out in order to describe better the wave-breaking process and to relate it to the generation of turbulence in the ocean and atmosphere. As was described in these papers, the amplitude of growing internal waves will be limited to some critical value above which local unstable density gradients will be produced. Because of the high Rayleigh numbers that normally exist in such geophysical situations as well as in the laboratory cases considered here these density anomalies will collapse in a turbulent manner, thereby producing small-scale turbulence and transforming wave energy into energy associated with this turbulence. We will assume here that the generation of turbulence due to this gravitational instability is independent of the manner in which the unstable density gradient was produced. This decoupling of local instability processes from the phenomena with larger scales producing the instability greatly facilitates the parameterization of subgrid scale mixing, since we may then relate the amount of local turbulence generation to local properties of the flow field. In fact, we will treat the gravitational instability process as an isolated event in space and time, regardless of whether the unstable density gradient occurring in the flow field was the result of gravity wave breaking or local heat transfer processes (such as free convection occurring near the lower boundary of the atmosphere because of solar heating).

It should be emphasized that we only wish to parameterize instability processes that occur in length scales smaller than the numerical grid size. Any gravitational instability that can be resolved by the numerical grid resolution will be assumed to be adequately reproduced by the model. We will therefore seek to parameterize only the turbulence generation that may occur within subgrid scale regions of the model. We may visualize these regions as being equivalent to the grid boxes defined by adjacent horizontal and vertical grid points.

When a grid-sized region of the computational field becomes unstable, we will assume that turbulent mixing develops immediately and that turbulent transport within the grid box may be considered to be steady over the time interval of one time step Δt of the numerical model. This idealization of the convection process amounts to an assumption that the time required for the turbulent mixing process within the box to adjust to a change in the local unstable density gradient is much shorter than the model time increment Δt.

As regards the parameterization of subgrid scale quasi-steady convection in the model, two different approaches will be considered here in relating vertical heat (or density) flux to local temperature (or density) gradient. As was mentioned earlier, *Priestley* [1954] used dimensional analysis and the assumption that heat flux is independent of molecular diffusion coefficients in atmospheric convection to infer that heat flux depends on $(-\partial\theta/\partial z)^{3/2}$ and thus that eddy diffusivity κ_e depends upon $(-\partial\theta/\partial z)^{1/2}$ as given by (1) above. On the other hand, laboratory experiments [*Silveston*, 1958; *Globe and Dropkin*, 1959] and theoretical analysis [*Kraichnan*, 1962] concerning free convection without wind at high Rayleigh numbers show that nondimensional heat flux in the form of Nusselt number Nu is proportional to the $\frac{1}{3}$ power of Rayleigh number Ra (and thus $\kappa_e \propto (-\partial\theta/\partial z)^{1/3}$ is implied) for a given Prandtl number. *Ingersoll* [1966] has found experimentally that this result (as well as the proportionality of nondimensional momentum flux to $Ra^{1/3}$) continues to be valid in flows with weak velocity shear.

The differences between the two forms of temperature gradient dependence should not produce crucial differences in the behavior of the parameterization (and in fact the use of the two different formulations in some of the numerical calculations presented later has been

shown to produce qualitatively similar behavior). However, we feel that use of the Rayleigh number formulation with the implied dependence of convection fluxes on molecular diffusion properties of the fluid is the more appropriate of the two expressions in treating the initially laminar laboratory studies to be presented in the present paper. Also, in keeping with Ingersoll's results for convection with weak shear and in lieu of empirical results involving strong shear we will assume that

$$Nu = \alpha Ra^{1/3} \qquad (3)$$

where α is taken equal to 0.1 (Ingersoll found $\alpha = 0.08$). Here we are defining the Nusselt number Nu and the Rayleigh number Ra in terms of properties in a grid box of dimensions Δx by Δz:

$$Nu = \frac{\mathcal{3C}\Delta z}{\kappa_0 \Delta \theta} \qquad Ra = \frac{g\Delta\theta\Delta z^3}{\theta\kappa_0\nu_0} \qquad (4)$$

where κ_0 and ν_0 are molecular diffusivity and viscosity, respectively, g is the gravitational acceleration, and $\Delta\theta$ is the vertical unstable temperature difference across the grid box. (In flows involving moderate levels of turbulence it is possible to use this same parameterization but with the molecular values of κ_0 and ν_0 replaced by the constant background eddy diffusivity values that are assumed for the viscosity and diffusivity coefficients where density stratification is stable. This procedure has been used in studies of the planetary boundary layer by *Orlanski et al.* [1973].) The total vertical heat transport across the box is defined as

$$\mathcal{3C} = \kappa_0(\Delta\theta/\Delta z) - \langle w'\theta'\rangle \qquad (5)$$

Substituting (5) into the Nusselt number definition in (4), we may rewrite Nu as

$$Nu = 1 + (\kappa_e/\kappa_0) \qquad (6)$$

where we have defined the eddy diffusivity κ_e as

$$\kappa_e \equiv -\frac{\langle w'\theta'\rangle}{\Delta\theta/\Delta z} \qquad (7)$$

The empirical result (3) thus provides an expression for the eddy diffusivity due to subgrid turbulent convection when the temperature gradient is unstable. The total eddy diffusivity κ in a given grid box may then be calculated as follows:

$$\kappa \equiv \kappa_e + \kappa_0 = \kappa_0 \qquad \Delta\theta \geq 0$$
$$\kappa \equiv \kappa_e + \kappa_0 = \kappa_0\left(1 + \alpha\left(\frac{g\Delta\theta^{1/3}}{\theta\kappa_0\nu_0}\right)\Delta z\right)$$
$$\Delta\theta < 0 \qquad (8)$$

Ingersoll's experiments show nondimensional momentum flux to have a similar behavior to the Nusselt number. Thus we will assume for simplicity that eddy viscosity ν_e has the same dependence on Rayleigh number as κ_e.

Finally, it is important to note that the above eddy coefficients can only be strictly applied to vertical diffusion processes. In order to incorporate this parameterization into the numerical solution of the Navier-Stokes equations we must also include an expression for horizontal eddy coefficients. Lacking other information on which to base our model, we will assume that in the laboratory flows to be treated in this paper the horizontal and vertical coefficients are equal, that is,

$$\kappa_H \equiv -\langle u'\theta'\rangle/\theta_x = -\langle w'\theta'\rangle/\theta_z \equiv \kappa_e \qquad (9)$$

Fully adequate treatment of horizontal diffusion coefficients must await further studies of free convection with horizontal temperature gradients.

As can be seen from the above parameterization, the present formulation of eddy diffusivity and viscosity is highly selective in removing energy at locations of gravity wave breaking and free convection. We will demonstrate in the solutions that follow that energy dissipation is strongest in the high wave numbers; on the other hand, low wave numbers are left virtually unaffected until wave breaking occurs and modifies the entire flow field. We are thus able to calculate the development of a complex gravity wave field up to and beyond the point at which the waves exceed their critical amplitudes and wave breaking occurs.

MODEL DESCRIPTION

The numerical model described below has been designed to simulate the behavior of a two-dimensional stratified fluid in a rectangular container. In the examples treated in this paper the container has a rectangular cross section with width L and height H and is filled with a linearly stratified fluid so that the initial density

$\rho = \rho_0\{1 + \beta[z - (H/2)]\}$, where $\beta < 0$. The fluid is incompressible with the Boussinesq approximation assumed.

The condition of two dimensionality allows us to formulate the Navier-Stokes equations in terms of stream function ψ and vorticity ζ. The resulting equations may be written as follows:

$$\frac{\partial \zeta^*}{\partial t^*} = J^*(\psi^*, \zeta^*) + \frac{\partial \theta^*}{\partial x^*}$$
$$+ \frac{1}{Re} \nabla^*(\nu^* \nabla^* \zeta^*) \qquad (10)$$

$$\frac{\partial \theta^*}{\partial t^*} = J^*(\psi^*, \theta^*) - \frac{\partial \psi^*}{\partial x^*}$$
$$+ \frac{1}{RePr} \nabla^*(\kappa^* \nabla^* \theta^*) \qquad (11)$$

$$\nabla^{*2}\psi^* = \zeta^* \qquad (12)$$

where variables have been nondimensionalized by using the container height H as the length scale and the inverse of the Brunt-Vaisala frequency $(N = (-g\beta)^{1/2})$ as the time scale. Thus nondimensional variables (distinguished here by asterisks) are related to their equivalent dimensional variables as follows:

$$x^* = x/H \qquad z^* = z/H \qquad t^* = tN$$

$$\psi^* = \psi/(NH^2) \qquad \theta^* = \frac{g}{N^2 H} \cdot \frac{\rho - \rho_0}{\rho_0}$$

$$\nu^* = \nu/\nu_0 \qquad \kappa^* = \kappa/\kappa_0 \qquad (13)$$

where κ_0 and ν_0 are the molecular or background values of heat or salinity and viscosity, respectively.

The finite difference formulation of the above equations is identical to the scheme used by *Lipps* [1971] except for the method of solution of the Poisson equation and the inclusion of variable viscosity in the diffusion term. The key aspects of the model will be described briefly here; the reader is directed to Lipps's paper for more details of the method.

In order to reduce truncation error, flow variables are specified over a staggered grid throughout the field with ψ and ζ defined at points $(I\Delta x, J\Delta z)$ in a Cartesian grid system but with values of θ specified at $([I - 1/2]\Delta x, [J - 1/2]\Delta z)$. Spatial derivatives are centered to achieve second-order accuracy. The

Jacobians of vorticity and temperature use the *Arakawa* [1966] and *Lilly* [1965] formulations so as to avoid nonlinear instability.

Variable viscosity is incorporated into the model in a straightforward manner. When ψ, ζ, and θ are assumed to be defined at the points described above, the diffusion coefficients κ and ν are defined at the point $([I - 1/2]\Delta x, J\Delta z)$ so as to facilitate the computation of $(\theta_{I,J+1} - \theta_{I,J})$, the difference $\Delta\theta$ in the eddy diffusivity (8). For example, the simplest case $(\partial/\partial x) (\kappa \, \partial\zeta/\partial x)$ has the finite difference form:

$$\frac{1}{(\Delta x)} 2[\kappa_{I+1,J}(\zeta_{I+1,J} - \zeta_{I,J})$$
$$- \kappa_{I,J}(\zeta_{I,J} - \zeta_{I-1,J})] \qquad (14)$$

The other diffusion terms may be placed in an analogous form by the proper interpolation of viscosity values.

Time differencing in (10) and (11) is achieved by a centered or 'leapfrog' technique with the solution timewise-smoothed every 30 time steps to suppress time-splitting effects due to the leapfrog time-marching procedure. Diffusion terms are lagged one time step behind center in the three-level time-differencing molecule in order to improve numerical stability and to further inhibit time splitting.

To summarize the model description so far, we have described the general characteristics of the space and time differencing for (10) and (11) enabling us to advance ζ and θ from time step n to $n + 1$. However, in order to advance the solution to $n + 2$ we will require values for stream function ψ at $n + 1$. These are obtained by using the newly calculated values of ζ at time step $n + 1$ in the solution of the Poisson equation (12).

The method of solution of (12) uses a modification of the noniterative algorithm employed by *Lipps* [1971]. In the basic algorithm, the use of periodic boundary conditions in the x direction permits the representation of stream function and vorticity in terms of a Fourier series in sines and cosines. Thus, for example, stream function at the point $(I\Delta x, J\Delta z)$ would be written as

$$\psi_{I,J} = \sum_{l=0}^{NM/2} \hat{\psi}_{1J}{}^l \cos\left(2\pi l \frac{I\Delta x}{L}\right)$$
$$+ \sum_{l=1}^{NM/2-1} \hat{\psi}_{2J}{}^l \sin\left(2\pi l \frac{I\Delta x}{L}\right)$$

where $NM \equiv L/\Delta x$. Substitution of this series into the finite difference form of the Poisson equation then leads to a set of linear equations in J for each Fourier component $\hat{\psi}_{kJ}{}^l (k = 1, 2)$ in terms of $\hat{\zeta}_{kJ}{}^l$. The solution of these sets of equations by standard techniques [*Richtymer and Morton*, 1967, pp. 198–201], as well as the use of fast Fourier techniques to greatly reduce computations, allows the solution of the Poisson equation to be obtained directly and rapidly without recourse to iterative techniques.

In the present model of fluid motion within a container we have abandoned the use of periodic boundary conditions in favor of impenetrable walls with velocity slip (no tangential velocity shear) at $x = 0, L$. Such boundary conditions may be achieved by assuming $\psi = \zeta = 0$ at the two side boundaries; these boundary conditions have the additional advantage of serving as a vertical axis of symmetry, since they imply that the horizontal velocity component u and the horizontal derivative of the vertical velocity component w are zero along the boundary. (As is discussed later, we always will assume that $\partial\theta/\partial x = 0$ on side walls. These three conditions thereby imply a symmetry boundary condition.)

If such conditions as $\psi = \zeta = 0$ are imposed at $x = 0, L$ on the complete Fourier series representation of ψ and ζ, this imposition would have the effect of forcing all cosine components $\hat{\psi}_{1J}{}^n$ to be zero. In addition, the remaining sine modes must be complete sine waves with the largest possible horizontal wavelength equaling L. In order to improve model resolution and to permit the occurrence of waves of wavelength $2L$ we have thus changed the Fourier series to include half-wave modes and neglect cosine modes. Accordingly,

$$\psi_{I,J} = \sum_{l=1}^{NM} \hat{\psi}_J{}^l \sin\left(\pi l \frac{I\Delta x}{L}\right)$$

Such a representation allows sloshing of fluid from side to side within the container when the container and the computational region coincide as in the section on resonant forcing of standing internal gravity waves. In addition, this formulation will permit us to use this model directly to compute only half a flow field for problems such as those treated in the two sections following it, in which the solution is understood to be symmetric about the center of the experimental tank.

Further details regarding boundary condition treatment will be given in the succeeding sections in which we will describe the modeling of specific experiments.

RESONANT FORCING OF STANDING INTERNAL GRAVITY WAVES

Orlanski [1972] has studied the problem of the growth of two-dimensional internal gravity waves in a container of rectangular cross section. In this problem, wave growth is driven by a paddle located at the top of the container that resonantly forces a free mode of the stratified fluid. The gravity waves driven in this manner can be made to increase in amplitude to the point where wave breaking of the primary mode occurs.

Orlanski was able to study this problem by experimental, analytic, and numerical investigations, thereby providing several different ways to describe the resonant wave growth process. In the present section we will elaborate on this earlier numerical simulation and also will investigate the effects on the numerical solution of several different treatments of the diffusion terms. However, before proceeding to a discussion of the simulation results we will first describe the boundary conditions that were used in this problem.

The boundary conditions used on the rigid side and bottom walls of the container are chosen so as to simulate free velocity slip as well as an adiabatic heating condition. Thus we require that

$$\psi = \zeta = \theta_x = 0 \qquad x = 0, L$$
$$\psi = \zeta = \theta_z = 0 \qquad z = 0$$

The velocity slip condition $\zeta = 0$ was chosen in place of a no-slip condition in order to avoid the formation of a viscous boundary layer along the walls, because the coarseness of the grid mesh would not permit a proper resolution of such viscous boundary layers for the Reynolds numbers presently used in the model.

Paddle forcing on the top boundary is represented by a boundary condition on stream function:

$$\psi(x, H, t) = f_0 \sin \omega_0 t \sin\left(\frac{2\pi x}{L}\right) \quad (15)$$

with $\omega_0 = 2\pi/\tau$, where τ is the period of the

paddle forcing and equals $20N^{-1}$ in this case. This condition, as well as earlier conditions on the side and bottom walls, is identical to the boundary conditions used in the analytic perturbation solution of *Orlanski* [1972]. As a result we can expect the analytic and numerical solutions to follow each other quite closely until nonlinear effects in the numerical solution cause the two solutions to diverge. This will in fact be demonstrated in the comparisons that follow.

Finally, in order to complete the top wall boundary condition we assume that

$$\zeta = \partial\theta/\partial z = 0 \qquad z = H \qquad (16)$$

The approximate assumption that vorticity vanishes at this boundary is motivated by the fact that the stream function forcing amplitude f_0 is very small in comparison with the resonant growing stream function in the interior. In fact, since forcing of the interior fluid is achieved by imposing a prescribed small vertical motion along the top boundary, this vertical motion will interact with the predominantly horizontal motion of the growing standing wave eddies immediately below this boundary to produce complex local motions that cannot be accurately resolved by the grid resolution of the model. As a result, shallow eddies develop within a few grid points of the top boundary after some five paddle periods. The use of various other boundary conditions, including conditions that use Orlanski's first-order analytic solution with

$$\zeta(x, H, t) = -\left[\left(\frac{2\pi}{L}\right)^2 + \left(\frac{3\pi}{H}\right)^2\right]\psi(x, H, t)$$

did not correct this behavior. However, since these vortices were always confined to the region next to the top boundary and since the assumed boundary conditions accurately produced the desired interior forcing, we believe that this unresolved boundary behavior has little effect on the interior gravity wave development, which is of primary interest to us here.

Three numerical solutions will be described here, all three of which represent the same physical situation but each involves a different diffusive behavior. In the first treatment the viscosity ν and the salt diffusivity κ are assumed to be constant and equal to molecular values for salty water with $Re = N^2 H/\nu_0 = 2 \times 10^5$ and $Pr = \nu_0/\kappa_0 = 500$. Because the present model resolution of 120 points in the

vertical and 32 points in the horizontal is too coarse to simulate effectively diffusion effects for such small diffusion coefficients, we expect that this model will have only weak viscous effects, and we thus will refer to the resulting solution as the low-κ solution for convenience of reference in the discussion that follows. The second solution is similar to the first in using constant diffusion coefficients but with the Prandtl number reduced to $Pr = 1$; as a result, diffusivity κ is 500 times larger in this case than in the previous case. We will refer to this solution as the high-κ solution. In the third and final solution we use the eddy diffusivity formulation as described in the section on parameterization of subgrid scale gravitational instability. When the density stratification is stable, the viscosity and salt diffusivity are assumed to equal the small constant values of the low-κ solution. On the other hand, when the density stratification is unstable, the diffusion coefficients vary as $\kappa_0(1 + \alpha Ra^{1/3})$.

The analytic solution for the standing wave problem is obtained by expanding the solution in powers of the paddle forcing amplitude f_0 (equation 15), which is assumed to be small:

$$\psi = \psi_1 f_0 + \psi_2 f_0^2 + O(f_0^3)$$
$$\theta = \theta_1 f_0 + \theta_2 f_0^2 + O(f_0^3) \qquad (17)$$

Substituting these power series into the inviscid form of (10) and (11), we may then solve for the first- and second-order solutions to the initial value problem in which $\psi = \theta = 0$ at $t = 0$, and the boundary conditions are the same as those prescribed for the numerical models. The resulting solution given by *Orlanski* [1972, pp. 582–583, equations 4.7 and 4.8] will be compared with the numerical solutions in the analysis that follows.

Finally, experimental data was obtained by *Orlanski* [1972] for the growth of the wave displacement amplitudes as a function of time in the standing wave configuration. Unfortunately, the paddle forcing amplitude, as well as the paddle geometry (two pivoting linear segments instead of the cosinusoidal shape assumed in the theoretical models), does not match the forcing function used in the theoretical models. However, qualitative comparisons are still possible and will be made in the discussion that follows.
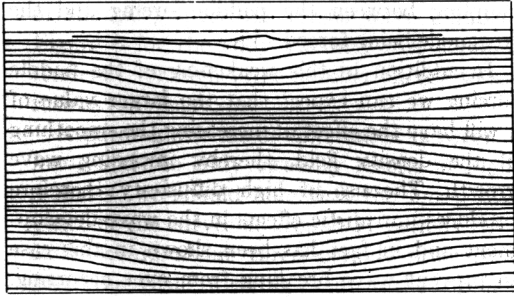
Fig. 1. Density contours at the time of maximum isopycnic displacement $tN = 124.$ from the standing wave solution with constant low diffusion coefficient κ. The graph at the top of the frame shows the amplitude of the stream function forcing along the top boundary.

Figures 1 and 2 show examples of the density and stream function fields at an early stage in the gravity wave growth. Figure 1 shows the density field after six paddle periods at the instant when the amplitude of the disturbance in the lower portion of the container is maximum. The accompanying Figure 2 displays stream function contours a quarter of a paddle period after the density disturbance maximum, at which time the stream function is maximum. Because diffusion and nonlinear effects are small in the solution at this time, the three numerical solutions and the analytic solution all produce results that are virtually identical to those shown in the figures.

The maximum values of stream function and temperature perturbation for each successive half period of the paddle forcing provide us with a valuable method for comparing the numerical and analytic solutions. In Figure 3 we have plotted the average of the bottom and middle stream function maximums as a function of time for the analytic solution and the three numerical solutions. As for density we have chosen to plot maximum isopycnic displacement instead of maximum density perturbation, because the former quantity was measured by Orlanski in his experimental investigation of standing wave growth. By isopycnic displacement we mean the following: Any given isopycnic, designated here by I, has a maximum height z_{I2} and a minimum height z_{I1} above the container bottom. If we form a sequence of differences $\delta_I = |z_{I2} - z_{I1}|$ for consecutive isopycnics, there will be local maximums in δ_I,
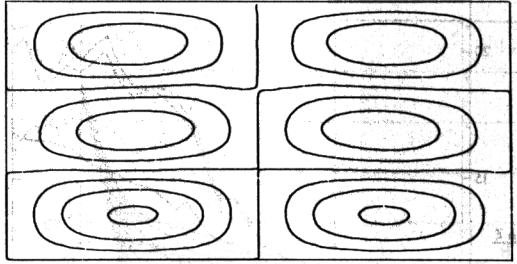

Fig. 2. Stream function contours from the standing wave solution with constant low κ at the time $tN = 130.$, when amplitudes are maximum.

for $I = I^*$ say, such that $\delta_{I^*} > \max (\delta_{I^*+1}, \delta_{I^*-1})$. It is these local maximums δ_{I^*} that we call maximum isopycnic displacements δz. In Figure 4 we plot the averages of successive time maximums of the maximum isopycnic displacements for the middle and bottom modes of the theoretical and experimental results. Isopycnic displacement data were obtained by a computerized form of the above algorithm for the numerical and analytic results and by measurement of dye line heights in tank photographs for the experimental results.

A study of Figures 3 and 4 reveals the time span over which the analytic solution is valid
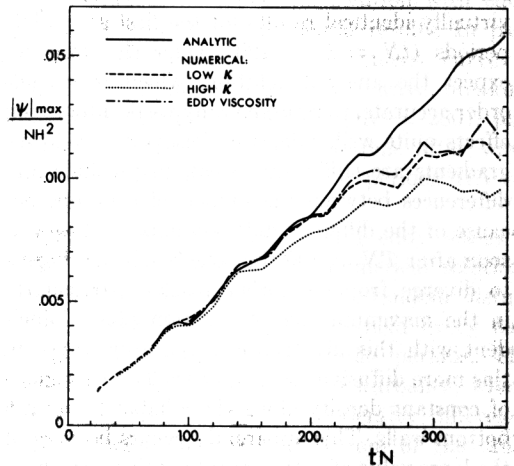

Fig. 3. Graph of the magnitudes of nondimensional stream function maximums versus nondimensional time from the analytic and numerical solutions. Stream function maximums represent the average of the peak values occurring in the bottom and middle eddies of the calculation field. One period of the paddle forcing equals $20\ N^{-1}$.
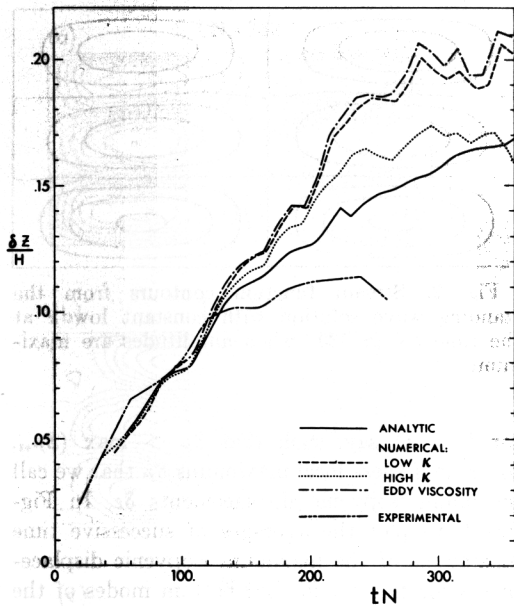
Fig. 4. Graph of nondimensional maximum isopycnic displacement versus nondimensional time from analytic, numerical, and experimental results. Analytic and experimental results are from *Orlanski* [1972].

as well as show the points in the wave growth process where larger diffusivity and major wave breaking become important. Both figures show the analytic and numerical solutions to give virtually identical results for the first six paddle periods ($tN = 0 - 120$). Over this time we expect the analytic solution, which is second-order accurate, to represent any weak interaction effects quite well. Likewise, density and velocity gradients are sufficiently weak to preclude any differences between the numerical solutions because of the different diffusion effects. However, soon after $TN = 120$ the large κ solution begins to diverge from the other results, particularly in the maximum stream function plot. Coincident with this divergence is the appearance in this more diffusive solution of thickening regions of constant density along the adiabatic top and bottom walls. This apparently occurs because of the large value of κ_0 that rapidly diffuses the constant density layers produced along the model walls due to the boundary condition $\partial\theta/\partial z = 0$. The growth of these constant θ regions has the effect of reducing the height of the stratified fluid in the container, thereby altering the free modes of the fluid and eliminating the resonant

coupling between the paddle forcing and the free mode being forced.

In addition to this weakening of the paddle forcing we can expect that the larger value of κ will have the effect of increasing the smoothing of the density field, thereby impeding wave growth. The use of high diffusivity therefore produces unrealistic effects in the wave development and in fact has been shown in this case to prevent wave breaking from ever occurring. On the other hand, the use of constant density boundary conditions on the top and bottom walls to prevent the formation of the constant density region always led to unstable solutions because of its apparent incompatibility with the paddle forcing on the top wall.

Around a time of six periods ($tN = 120$), when the large κ solution diverges, the curve of maximum isopycnic displacement for the analytic solution begins to diverge from the remaining two numerical solutions. However, the corresponding analytic curve for maximum stream function is seen to remain close to the two numerical solution curves until ten paddle periods ($tN = 200$). This difference between density and stream function results can be explained by the form of the analytic solution. As *Orlanski* [1972] has pointed out and as can be seen from equtions 4.7 and 4.8 of his paper, nonlinear interaction does not appear in the stream function solution until third order in f_0, whereas density shows a second-order interaction. Thus we would expect, and Figure 3 shows, that stream function is less sensitive than density to nonlinear effects. Nonlinear interaction is shown by the figures to have the effect of reducing the stream function growth and increasing isopycnic displacement until wave breaking occurs.

Finally, if we follow the growth of the low-κ and the eddy viscous solutions, we see that the two solutions show quite similar results for maximum stream function and isopycnic displacement over the duration of the comparison. We may conclude from this similarity that eddy viscosity effects have only a weak influence on low wave number properties such as these. On the other hand, small-scale overturning is filtered very effectively by the eddy viscosity formulation as is shown by the comparison in Figure 5 of the isopycnic fields at 18 paddle periods without and with eddy viscosity. Similarly, the plot

of the $\langle\theta^{*2}\rangle$ spectrum versus wave number in Figure 6 for the eddy viscosity case shows the tendency for high wave number energy to saturate as time increases.

Regarding the small differences between the low-κ and the eddy viscosity results in Figures 3 and 4, we should note that the initial divergence of the curves at around 11 periods ($tN = 220$) occurs about three periods prior to the first large-scale breaking event in the top of the container. This divergence can be explained by the occurrence of small-scale overturning in the upper region at this early time. Large differences between the solutions do occur at around 14 periods ($tN = 280$) with large-scale breaking in the top and at 16 periods ($tN = 320$) in Figure 4 when breaking in the bottom first appears.

Experimental isopycnic displacement data is also plotted in Figure 4. As was mentioned earlier, we have not attempted to match the paddle forcing amplitude in the theoretical solutions with that used in the physical experiment.
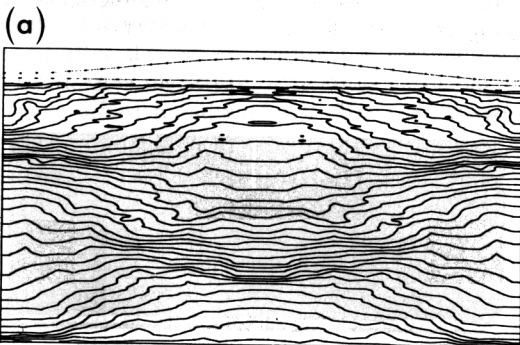
(a)

(b)
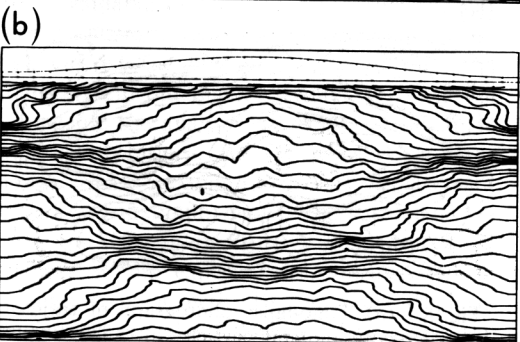
Fig. 5. Comparison of density contour plots at time $tN = 356.$ from standing wave solutions with (a) constant low diffusion coefficient κ and (b) eddy diffusion coefficients as described in the section on parameterization of subgrid scale gravitational instability.
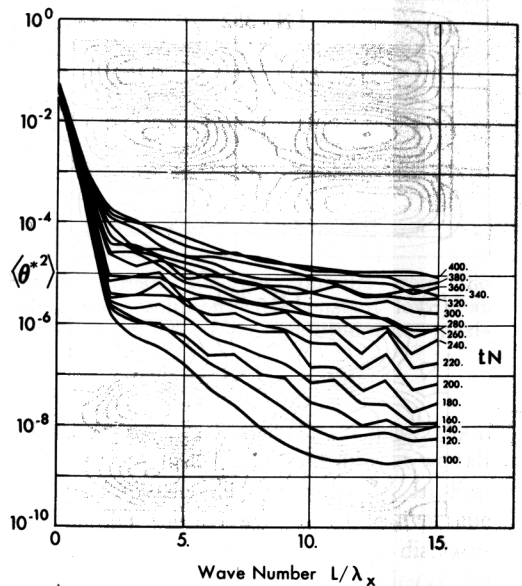

Fig. 6. Graph showing the spectrum of effective perturbed energy $\langle\theta^{*2}\rangle$ versus wave number L/λ_x. The quantity $\langle\theta^{*2}\rangle$ is averaged over five equidistant levels in z over the tank height with this quantity then averaged over one paddle period. The nondimensional time corresponding to each curve is given to the right of that curve.

We can, however, note the qualitative similarities between the numerical solution with eddy viscosity and the experimental results. In particular, the numerical displacement curve is seen to flatten out soon after wave breaking occurs at around 14 periods ($tN = 280$), just as the experimental curve flattens after wave breaking at approximately 10 periods ($tN = 200$).

The numerical solution with eddy viscosity differs from the other two numerical solutions in that it was perturbed by a random disturbance over the entire density field every half period beginning at 4.5 paddle periods. The maximum amplitude of this disturbance, which was less than 0.01% of the density difference βH between the top and bottom of the tank, was so small as to leave the mean solution properties unaffected. However, the random disturbance will excite asymmetric modes in the solution. (If such asymmetric modes were not introduced into the model in this manner, the numerical solution would remain perfectly symmetric for the entire calculation.)
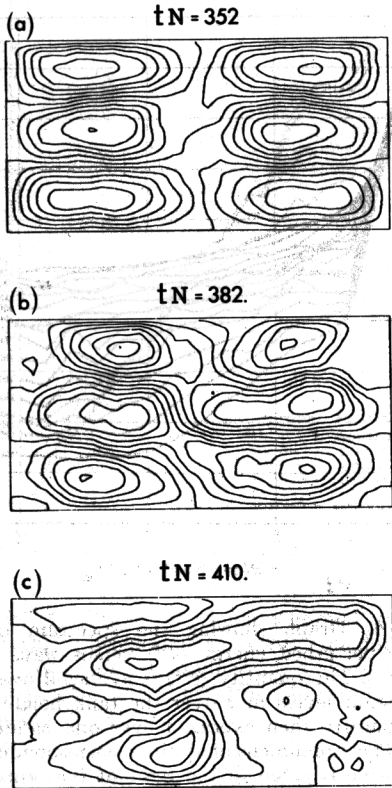
Fig. 7. Plots of stream function contours from the standing wave solution with eddy viscosity and with small random perturbations imposed every half period begining at $tN = 90$. The three cases shown correspond to times when stream function is maximum in time at some point within the field.

During the early stages of the solution prior to wave breaking, no asymmetry is evident in the solution. However, as density gradients steepen prior to the occurrence of wave breaking, the density field becomes more susceptible to the small magnitude disturbances, and slight asymmetries begin to appear. The isopycnics in Figure 5 show evidence of this asymmetry, whereas the stream function plot in Figure 7a at $15\frac{1}{2}$ periods shows a more pronounced effect in the region where stream function gradients are small.

The quality of the numerical solution can be expected to deteriorate after 18 periods as the amount of energy in the small scale increases. However, the use of the present eddy viscosity serves to dissipate much of this energy and allows us to follow the further growth of the

solution asymmetries. Figure 7(b and c), showing stream function fields at 19 and $20\frac{1}{2}$ periods, reveals the existence of a horizontal wave number $L/\lambda_x = \frac{1}{2}$, where previously the lowest wave number, the forcing function wave number, $L/\lambda_x = 1$.

The formation of a half wave number mode was observed experimentally by *Orlanski* [1972] by means of time-lapse photography of the circulation of neutrally buoyant particles in the stratified wave tank after wave breaking occurred (Figure 8a). An analogous field of trajectories has been obtained for the numerical solution by calculating the trajectories of tracers that are advected by the time-varying numerical solution. One such trajectory field, obtained from the numerical solution at $22\frac{1}{2}$ paddle periods, is displayed in Figure 8b below the experimental photograph and shows the great similarity that exists between the numerical and the experimental flow fields. (Compare also the similarity in low wave number development between the stream function plots of Figure 7 and the successive trajectory photographs of *Orlanski* [1972, Figure 14, Plate 5]).
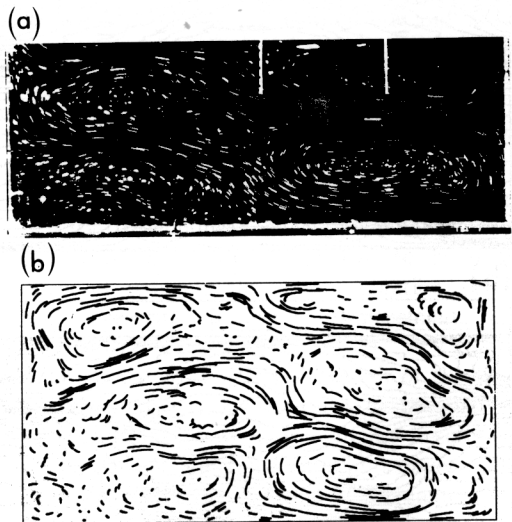

Fig. 8. (a) Time-lapse photograph of trajectories of neutrally buoyant particles in the lower part of an experimental tank in the standing wave experiment of *Orlanski* [1972] ($tN = 561.$). (b) Similar trajectory plot obtained from the numerical solution with eddy viscosity at $tN = 450$. The two trajectory fields show the shapes of the asymmetric flow fields to be quite similar.

COLLAPSE OF A MIXED REGION IN A
STRATIFIED FLUID

A number of other stratified fluid experiments can be simulated by using the present two-dimensional model with rectangular tank geometry. The two cases described in this and the next section involve the generation of traveling internal gravity waves caused by the transient deformation and motion of a nearly homogeneous bubble immersed in the stratified fluid. In each of the two calculations the fluid motion and the density field in the tank are assumed to be symmetric about a vertical center line passing down the middle of the tank. The numerical calculations will thus be carried out only for the right half of the tank with the left and right boundaries of the calculation field corresponding to the center line of the tank and right wall, respectively. The actual tank will be considered to have a width L that is 4 times its height H.

In this section we will discuss the simulation of the collapse of a two-dimensional mixed region immersed in a stratified fluid. Such a simulation provides us with an opportunity for comparing solutions from our numerical model with experimental as well as other numerical results. *Wu* [1969] has performed an experiment to study the internal wave generation due to the

collapse of a mixed region, such as would be generated by large eddies in the ocean. In this experiment, Wu enclosed a fluid of uniform density in a half-cylindrical container mounted on the left side wall of a rectangular tank of fluid having a stable density stratification. (As in our numerical model, Wu chose an experimental configuration that represents only the right half of the tank, which would be required if the mixed region were placed in the center of the fluid.) At time $t = 0$ the container enclosing the mixed fluid is removed, and the uniform fluid, which has no net buoyancy in the stratified fluid, begins to collapse. Internal waves generated by the deforming fluid element radiate away from the element as the mixed region collapses. The inclination and the horizontal position of the wave rays change with time as the shape of the element changes and the wave fronts propagate. Wu determined the inclination and horizontal position (relative to the top of the uncollapsed mixed region) of these rays by marking the wave crests and troughs as observed from fluid dye lines in successive ciné photographs of the tank. The dots in Figure 9 show Wu's results for the ray inclination to the horizontal plotted against the ratio x/R. The x is the horizontal distance from the center
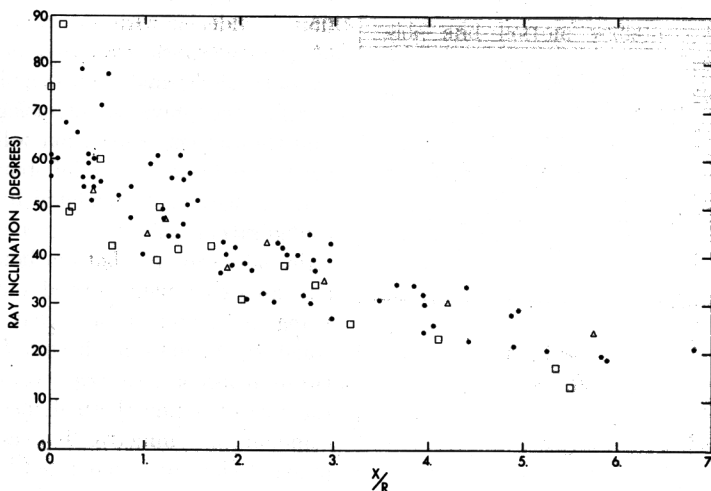

Fig. 9. Graph showing the inclination of gravity wave rays to the horizontal versus non-dimensional distance x/R as obtained from experimental and numerical results for the collapse of a mixed region. The length x is the horizontal distance from the center line at which a ray intersects the horizontal line marking the initial height of the top of the mixed region prior to its collaspse; R is the initial radius of this mixed region. Data are shown from the experimental results of *Wu* [1969] (dots), from the numerical solution by *Young and Hirt* [1972] (triangles), and from the present numerical solution (squares).

line to the point at which the ray crosses the level of the top of the undisturbed mixed region. The R is the initial radius of the mixed region at time $t = 0$.

The present model has been adapted to the problem of the collapsing mixed region by replacing the stream function forcing at the top boundary by a rigid lid and by introducing the half circle of uniform density fluid along the left boundary of the field at time $t = 0$. The eddy viscosity term used previously has been included in the present calculation but causes virtually no change in the numerical solution. (Maximum changes were less than 2% in vorticity and perturbation density). This is reasonable, since the only significant overturning that may appear in the field should occur above the mixed region as the fluid first collapses, and this overturning appears to be quite weak.

Comparison is made in Figure 9 of the ray inclination results obtained from our numerical solution, from the experimental results of Wu, and from the numerical solution of *Young and Hirt* [1972]. The latter numerical solution was obtained with a marker-and-cell model that is quite similar to the present model but that involves the primitive equations instead of the

vorticity formulation employed here. As the figure shows, both numerical solutions give data within the range of scatter of the experimental data.

The locations of wave crests and troughs obtained from our numerical model for use in the data of Figure 9 were determined from plots of perturbation density such as that shown in Figure 10b. The crests and troughs shown in Figure 10a do not correspond to the apparent axes of the tongues of maximum and minimum perturbation density, respectively; rather the loci of the points of greatest and least height along each line of constant perturbation density represent the crests and troughs in the corresponding plot of isopycnics. By using these perturbation contour plots we are able to identify effective crests at inclinations up to 88° near $x = 0$, as shown in Figure 9.

PENETRATION OF AN ISOLATED THERMAL INTO A
STABLY STRATIFIED FLUID

An interesting geophysical phenomenon that is amenable to the stratified tank configuration is the rising of a buoyant fluid element in a stably stratified environment and the ensuing generation of internal gravity waves as the bubble oscillates and collapses at its neutrally buoyant height. The magnitude of the gravity wave field generated by such bubble penetration provides us with insight into the magnitude of gravity waves generated in the atmosphere by isolated thermals and cumulus clouds.

As in the previous collapsing bubble simulation the present calculation will employ a symmetry condition on the left boundary with only half the flow field calculated by the model. The configuration will use slip boundaries on the right side, top, and bottom boundaries to simulate an experiment carried out with a bubble rising in the center of a tank with a length L equal to 4 times its height H. The model is two-dimensional, so that we will be modeling the rise of a line thermal instead of the more common axisymmetric buoyant element. The buoyant element is generated by prescribing the temperature by Gaussian functions in t and x along the bottom boundary as follows:

(a)

(b)

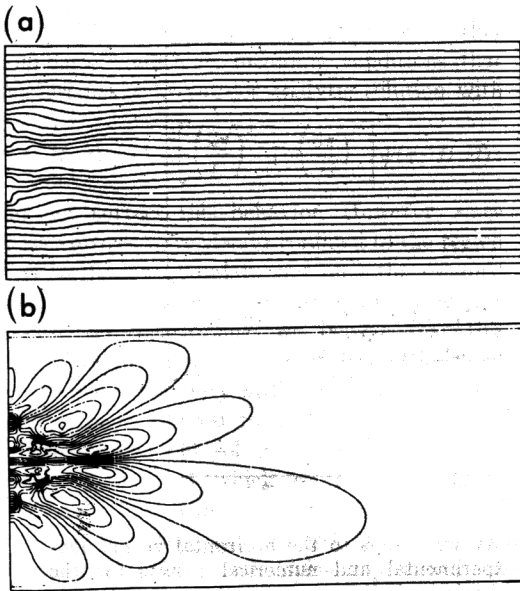
Fig. 10. (a) Plot of density contours at time $tN = 15$. during mixed region collapse, and (b) the corresponding plot of perturbation density contours.

$$\theta^*(x, 0, t) = -0.50\left(1 - \exp\left\{-\left(\frac{x}{1.2H}\right)^2 - \left(\frac{10 - tN}{40}\right)^2\right\}\right)$$

where the initial stratification in the interior varies linearly as $\theta_o^* = -0.5 + z/H$. The amplitude of the Gaussian temperature distribution changes from 0.94 times its maximum at $tN = 0$ to its maximum value at $tN = 10$. The peak temperature at $x = 0$ at this latter time is equal to the ambient temperature at $z/H = 0.5$. Following this maximum the boundary temperature decays to the initial ambient value $\theta_o^*(z = 0) = -0.5$. In this way we simulate the generation of an isolated thermal by a transient localized temperature maximum occurring on the bottom boundary of a laboratory tank.

The method of parameterization of eddy viscosity is critical to the successful simulation of gravity wave generation by penetrative convection. The use of an eddy viscosity coefficient, which is far larger than the molecular viscosity of water, is necessary in order to parameterize the turbulent mixing present as the bubble rises and dissipates. However, the use of a constant coefficient has been shown by numerical experiment to be unsatisfactory in the present problem because the large viscosity required not only retards the bubble motion but also damps out oscillations in the stable region above the bubble, thereby preventing the generation of internal gravity waves. On the other hand, the use of an eddy viscosity formulation, which is proportional to the local magnitude of the unstable temperature gradient, provides a large viscosity in the turbulent bubble region, whereas it imposes nearly inviscid conditions in the stable gravity wave field above the mixed lower layer (with the exception of the regions where gravity wave breaking occurs). The eddy viscosity as formulated in the section on parameterization of subgrid scale gravitational instability is therefore well suited to penetrative convection processes and will be used in the numerical solution of the present problem.

Figure 11 shows the sequence of isotherm fields with the creation and decay of the bubble and with the resulting generation of internal waves in the stable fluid above. Below each contour plot is a graph showing the current temperature distribution occurring along the bottom boundary of the field. The first frame shows the early effects of bottom heating as the Gaussian temperature function first grows. As the heated fluid rises further, it 'necks down'

to form a circular cap $(tN = 10.)$ with the influence of the line vortex below and to the right of the cap shown by the tongue of cooler fluid curving behind the cap in a manner similar to that described by *Woodward* [1959]. The topmost portion of the cap reaches its peak penetration $z/H = 0.63$ at $tN = 14$. soon after the time $tN = 10$. of maximum temperature at the bottom boundary. Since the peak temperature imposed at the bottom boundary corresponds to the ambient temperature at the height $z/H = 0.5$, the buoyant cap has clearly overshot its neutral height and must fall back.

At time $tN = 14$. the bubble has achieved its maximum height. The remnant of cooler
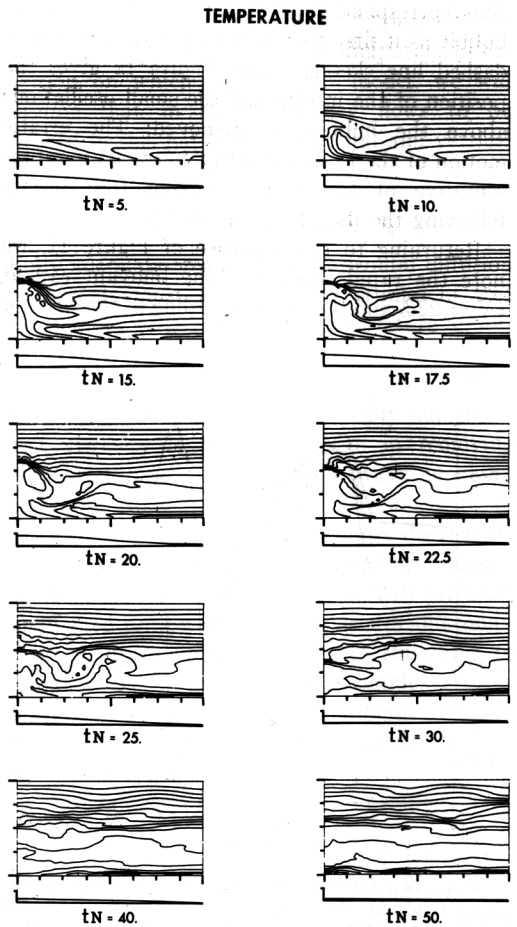
TEMPERATURE

Fig. 11. Sequence of temperature contour plots during the rise and collapse of the buoyant bubble. Graphs showing the amplitude of the imposed temperature forcing along the bottom boundary of the field are given below each frame.

fluid seen as a closed contour below the limb of the cap was drawn into the bubble by the clockwise vortex during the rise of the bubble. Now with the upward motion stopped the sense of the vorticity under the limb has reversed, and the fluid under the cap is beginning to spread downward and away from the center line.

A more detailed picture of the vertical motion of the bubble can be obtained from Figure 12, in which the heights along the center line $x = 0$ of the two isotherms θ^* equal to -0.05 and 0.05 (initially at $z/H = 0.45$ and 0.55, respectively, in the undisturbed field) are plotted against time. Both of these isotherms are located in the interface above the buoyant cap at time $tN = 15$. in Figure 11. Their motion should thus correspond roughly to the motion of the bubble as it first rises and falls back. The heavy dashed line sketched into Figure 12 gives the position of the interface if the small oscillations above the bubble are removed. The erratic motion of the isotherms after $tN = 25$ is representative of the violent mixing that occurs following the descent of the bubble.

Returning to the sequence of Figure 11, we note the rapid sinking of the buoyant cap at $tN = 22.5$ and the swift spreading of the warmer
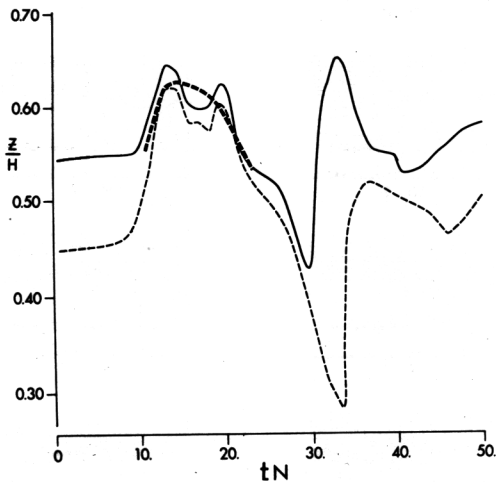

Fig. 12. Graph showing the nondimensional height along the center line of two isotherms $\theta^* = 0.05$ (solid line) and $\theta^* = -0.05$ (light dashed line) versus time. Both isotherms are located within the interface above the bubble during its initial rise. The heavy dashed line designates the approximate trajectory of the interface if high-frequency buoyancy oscillations are neglected.

fluid from the collapsing bubble into the stratified region to the right. The outward motion is sufficiently violent to produce the overturning shown in the center of frame $tN = 25$. The subsequent contour plots in Figure 11 show a greatly reduced mixing with the stratification in the lower half of the field now reduced to one fourth of its initial value.

Up to this point the discussion has concentrated on the motion of the bubble and the resulting mixing in the lower half of the field. However, another matter of great interest is the determination of the extent to which the motion of a thermal can generate internal gravity waves in the stably stratified fluid above it. Although the results of the present calculation are of limited generality because of the influence of the tank boundaries on the internal wave development, they still can provide an indication of the length scales and the amplitudes of the internal wave field that can be generated by a bubble of the magnitude considered here.

The temperature contours in Figure 11 show internal gravity waves in the upper half of the field as the bubble rises and begins to sink. It is difficult to discern details of the internal wave field from these contour plots. Therefore in order to show more clearly the amplitude and period of the wave field we have plotted in Figure 13 a time history of the temperature perturbations at various horizontal positions across the calculation field and for three heights within the stratified region above the bubble. The bubble in fact penetrates one of these height levels as shown by the large drop in temperature around the time $tN = 11$. at the point $x/L = 0$. and $z/H = 0.56$. Oscillations also occur soon after $tN = 10$. at all other stations but only become strong after $tN = 15$. as the bubble begins to drop. At $tN = 30$ the tongue of fluid spreading from the collapsing bubble protrudes up into the stable layer (see Figure 11, $tN = 22.5, 25., 30.$) in the center of the field at station $x/L = 0.26$ to set off a second disturbance generating large amplitude internal waves. A survey of the time traces in the figure shows wave frequencies in this field ranging between $0.6N$ (lower frequencies are present in the figure but are difficult to identify because of the transience of the phenomena and the shortness of the observation period) and N, oscillations of $0.8N$ being most pronounced.
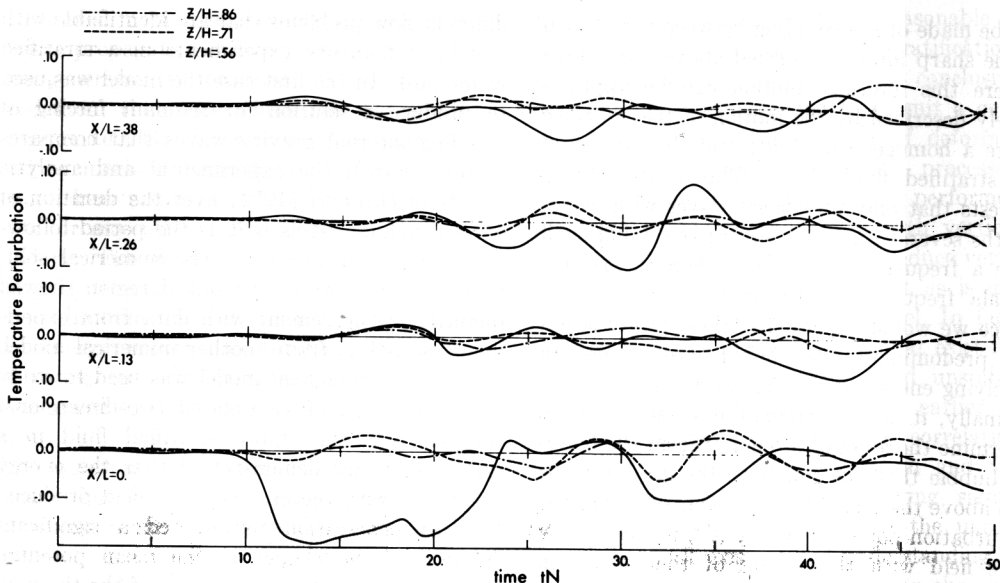
Fig. 13. Graphs showing temperature perturbations versus time at three different heights for four horizontal positions. All points are located within the upper stable region in which gravity waves are generated by the penetration of the bubble.

Oscillations close to the Brunt-Vaisala frequency are localized to the region immediately above locations of strong forcing, namely, the regions above the penetrating bubble at $tN = 10$ (note the oscillations of isotherms in Figure 12 at this time) and above the penetrating tongue of fluid in the center of the tank at $tN = 30$. The frequencies around $0.8N$ as well as the lower frequencies observed represent gravity waves excited by lower harmonics of the initial penetration of the bubble into the stable layer as well as by the later interaction of the stable layer and the mixed layer below.

The dominant horizontal wavelengths of the gravity wave field can be seen from the power spectrum in Figure 14 of squared temperature perturbation averaged over the time interval $tN = 25$–50 after the bubble has collapsed. The wavelengths λ_x equal L and $L/2$ are seen to predominate even though the bubble scale is approximately $L/4$ (as shown in Figure 14 by the peak in the mean-squared spectrum of perturbation height z'/H of an isotherm within the bubble interface at maximum bubble penetration). At first sight this energy accumulation in tank-sized scales would appear to be due only to the influence of tank boundaries on the developing wave field. However, further analysis
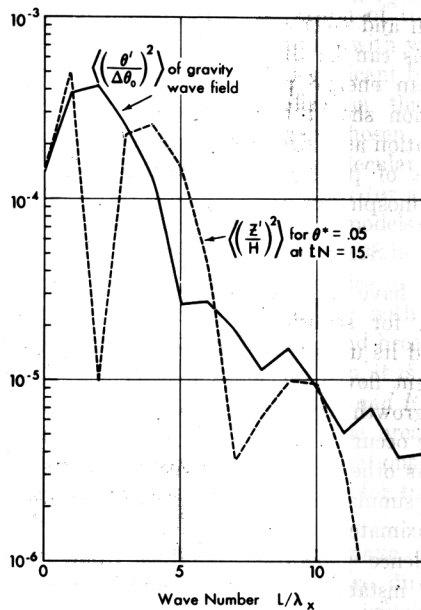

Fig. 14. Graph showing the spectrum of the mean square of the nondimensional perturbation temperature $\langle (\theta'/\Delta\theta_0)^2 \rangle$ averaged over three heights in the gravity wave field above the collapsing bubble and averaged over the time interval tN from 25. to 50.; also the mean square of the nondimensional perturbation height $\langle (z'/H)^2 \rangle$ for the isotherm $\theta^* = 0.05$ located in the bubble interface and taken at the time $tN = 15.$, when bubble penetration is maximum.

can be made of the coupling between the motion of the sharp interface formed above the bubble (where this interface motion can be approximately described by the motion of the interface above a homogeneous fluid) and the motion of the stratified fluid above. This simple model suggests that only interfacial waves with wavelengths several times the size of the bubble will have a frequency that is less than the Brunt-Vaisala frequency of the stable region above. Hence we would expect that these larger scales will predominate over bubble-sized scales in supplying energy to the gravity wave field.

Finally, it is of particular interest for us to determine the amount of energy from the buoyant bubble that has gone into the gravity wave field above the mixed layer. A comparison of the perturbation potential energy $\langle \theta'^2 \rangle$ in the gravity wave field with the square of the change in mean temperature $(\langle \theta \rangle - \langle \theta_0 \rangle)^2$ averaged over the entire tank shows that energy in the gravity wave field is 12% of the change in mean potential energy in the tank owing to the bubble generation and collapse. Although no general conclusions can be drawn from this single study, such an energy partition suggests that more attention should be directed to gravity wave generation as a significant element in the energy budget of penetrative convection processes in the atmosphere.

SUMMARY AND CONCLUSIONS

We have described here a finite difference model for stratified fluids and have demonstrated its use in the simulation of a variety of different flow phenomena in which the generation, growth, and overturning of internal gravity waves occur. The modeling of wave breaking as well as other forms of convective instability in these simulations is made possible through an approximate parameterization of the subgrid turbulence generation resulting from gravitational instability. In this formulation the local magnitude of eddy viscosity, and thereby the turbulent mixing, within unstable regions is assumed to be a function only of the gravitational instability as expressed by the local Rayleigh number. The effect of velocity shear, such as might occur during wave breaking, is assumed to be of only secondary importance and is therefore neglected.

Numerical solutions were carried out for three different flow problems that are identifiable with possible laboratory experiments in a stratified water tank. In the first case the model was used to produce a solution for resonant forcing of standing internal gravity waves that compares favorably with the experimental and analytic results of *Orlanski* [1972] over the duration of wave development as well as the period following initial wave breaking. The numerical solution for the collapse of a mixed region showed quantitative agreement with data from experiment as well as from another numerical model. Finally, the numerical model was used to study the penetration of an isolated two-dimensional thermal into the stably stratified fluid in a water tank and demonstrated that the energy associated with the gravity wave field produced by this penetration represented a significant fraction of the change in the mean potential energy produced by the creation of the thermal.

We have thus demonstrated that the present finite difference model in conjunction with the parameterization of subgrid scale turbulence generation provides an effective tool for studying stratified fluid phenomena in which stably stratified regions with laminar flow or with flow having only moderate turbulence levels are interspersed with regions of high mixing rates caused by convective instability. Many mesoscale and intermediate scale geophysical flows will consist of such a mixture of gravitationally stable and unstable regions. The proper interaction of these regions and the correct representation of gravity wave generation sources such as the penetrative convection mechanism treated in the preceding section are important phenomena that should be present in any numerical model of atmospheric or oceanic mesoscale flow.

However, in order to extend the model to more relevant geophysical problems one must recognize the weakness of using our assumption of equality between vertical and horizontal eddy diffusion coefficients for mesoscale flows; for, although this assumption appears to be reasonable for laboratory scale models in which vertical and horizontal motions are of the same order of magnitude, it will be less valid for mesoscale geophysical problems in which the ratio of horizontal to vertical eddy scales is much greater than unity. A more realistic relationship between horizontal and vertical diffus-

sion coefficients should thus be developed in order to account for the differences in the corresponding eddy scales.

We are now in the process of transforming the model into a form that is suitable for the study of mesoscale atmospheric phenomena. Preliminary results from a city scale version show good agreement of solution characteristics, such as planetary boundary layer thickness, with observational results. Details of this model will be presented in a forthcoming paper.

A film showing the growth and breaking of standing internal gravity waves has been developed by the authors using the present numerical model as well as laboratory experiments and is available from the authors upon request.

REFERENCES

Arakawa, A., Computational design for long term numerical integration of the equations of motion: Two dimensional incompressible flow, 1, *J. Comput. Phys., 1,* 119–143, 1966.

Daly, B. J., and F. H. Harlow, Transport equations in turbulence, *Phys. Fluids, 13*(11), 2634–2649, 1970.

Deardorff, J. W., Three-dimensional numerical modeling of the planetary boundary layer, in *Workshop on Micrometeorology,* edited by D. A. Haugen, pp. 271–311, American Meteorological Society, Boston, Mass., 1973.

Globe, S., and D. Dropkin, Natural convection heat transfer in liquids confined by two horizontal plates and heated from below, *J. Heat Transfer, 81,* 156–185, 1959.

Gossard, E. E., J. H. Richter, and D. Atlas, Internal waves in the atmosphere from high-resolution radar measurements, *J. Geophys. Res., 75,* 3523–3526, 1970.

Hooke, W. H., J. M. Young, and D. W. Beran, Atmospheric waves observed in the planetary boundary layer using an acoustic sounder and a microbarograph array, *Boundary Layer Meteorol., 2,* 371–380, 1972.

Ingersoll, A. P., Thermal convection with shear at high Rayleigh number, *J. Fluid Mech., 25*(2), 209–228, 1966.

Kraichnan, R. H., Turbulent thermal convection at arbitrary Prandtl number, *J. Fluid Mech., 25*(2), 209–228, 1962.

Lilly, D. K., On the numerical simulation of buoyant convection, *Tellus, 14*(2), 148–172, 1962.

Lilly, D. K., On the computational stability of numerical solutions of time dependent nonlinear geophysical fluid dynamics problems, *Mon. Weather Rev., 93,* 11–26, 1965.

Lilly, D. K., Wave momentum flux—A GARP problem, *Bull. Amer. Meteorol. Soc., 53*(1), 17–23, 1972.

Lipps, F. B., Two-dimensional numerical experiments in thermal convection with vertical shear, *J. Atmos. Sci., 28*(1), 3–19, 1971.

Orlanski, I., Energy spectrum of small scale internal gravity waves, *J. Geophys. Res., 76,* 5829–5835, 1971.

Orlanski, I., On the breaking of standing internal gravity waves, *J. Fluid Mech., 54*(4), 577–598, 1972.

Orlanski, I., The trapeze instability as a source of internal gravity waves, 1, *J. Atmos. Sci., 30*(6), 1007–1016, 1973.

Orlanski, I., and K. Bryan, Formation of the thermocline step structure by large amplitude internal gravity waves, *J. Geophys. Res., 74,* 6975–6983, 1969.

Orlanski, I., B. B. Ross, and L. J. Polinsky, Diurnal variation of the planetary boundary layer in a mesoscale model, submitted to *J. Atmos. Sci.,* 1973.

Priestley, C. H. B., Convection from a horizontal surface, *Aust. J. Phys., 7,* 176–201, 1954.

Richtymer, R. D., and K. W. Morton, *Difference Methods for Initial-Value Problems,* pp. 198–201, Interscience, New York, 1967.

Silveston, P. L., Warmedurchgang in waagerechten Flussigkeitsschichten, *Forsch. Geb. Ingenieurw., 24,* 59–69, 1958.

Smagorinsky, J., General circulation experiments with the primitive equations, 1, The basic experiment, *Mon. Weather Rev., 91*(3), 99–164, 1963.

Woodward, B., The motion in and around isolated thermals, *Quart. J. Roy. Meteorol. Soc., 85*(364), 141–151, 1959.

Wu, J., Mixed region collapse with internal wave generation in a density stratified medium, *J. Fluid Mech., 35*(3), 531–544, 1969.

Young, J. A., and C. W. Hirt, Numerical calculation of internal wave motions, *J. Fluid Mech., 56*(2), 265–276, 1972.